Calculation of band structures for surface waves in two-dimensional phononic crystals with a wavelet-based method

Zhi-Zhong Yan and Yue-Sheng Wang*

Institute of Engineering Mechanics, Beijing Jiaotong University, Beijing 100044, People's Republic of China
(Received 23 November 2007; revised manuscript received 3 August 2008; published 30 September 2008)

A wavelet-based method is developed to calculate the band structures of surface modes in two-dimensional phononic crystals including mixed fluid/solid systems and solid/solid systems with small or large acoustic mismatch. The defect modes of the surface waves are also calculated by using the supercell technique. The method is validated by recomputing the samples already studied in literatures. The results show some merits of the present method. In addition, the present method is applied to some new samples to show more properties of the surface modes. The influences of various factors, especially the acoustic mismatch, on the surface modes are discussed in detail. The present method may serve as an alternative method for studying the surface waves in general phononic lattices.

I. INTRODUCTION

Recently, the propagation of elastic or acoustic waves in the so-called phononic crystals,[1] which are made of two- or three-dimensional (2D or 3D) periodic repetition of two different solid or fluid constituents, exhibiting large contrast between their elastic constants and/or mass densities, has received considerable attentions.[2] The existence of elastic band gaps in such materials may lead to many potential applications such as sound shields, acoustic filters, transducers, refractive devices, wave guides, etc. Of particular interest for study of phononic crystals is achieving a complete frequency gap for mixed longitudinal and transverse-wave modes. So far, several methods have been developed to calculate the band gaps of bulk acoustic waves (BAWs) propagating in various materials combinations with small or large acoustic mismatch. Among all methods, three of them, i.e., the plane-wave expansion (PWE),[1] multiple-scattering theory (MST),[3] and finite difference time domain (FDTD) methods,[4] are widely used.

When a surface is introduced to break the periodicity of the system, a phenomenon of wave localization may appear, that is, under certain conditions, localized acoustic modes (usually termed surface acoustic waves or concisely SAWs) can propagate along the surface with their energy concentrated near the surface and their amplitude decreasing exponentially with depth. This topic is relevant to the design of new SAW devices and thus has received considerable attention. Tanaka and Tamura[5,6] performed detailed calculations for SAWs in a square lattice consisting of cubic materials (AlAs/GaAs) and in a triangular lattice consisting of isotropic materials (Al/polymer) using the PWE method. They also discussed the existence and features of the so-called pseudo-surface acoustic waves (PSAWs) that behave like SAWs but have a wave component slowly radiating their energy into bulk of the phononic crystal. The PSAWs attenuate very slowly with propagation distance because of weak coupling to a bulk shear wave mode. Tartakovskaya[7] estimated the first full band gap of SAWs in the phononic crystals of Ni/Al systems by employing a procedure similar to the so-called empty lattice of solid-state physics based on the plane-wave

expansion of the displacements. Wu *et al.*[8] presented detailed computation for band structures of SAWs in phononic crystals consisting of general anisotropic materials. Recently, both Tanaka *et al.*[9] and Sun and Wu[10] used the FDTD method to calculate the SAW modes in steel/epoxy phononic crystals having large acoustic mismatch. The propagation of SAWs through the straight and sharply bent waveguides was also studied. Wu *et al.*[11,12] fabricated a micromachined air or vacuum/silicon and an air/quartz phononic crystal[13] and conducted both theoretical and experimental researches. The temperature effect was considered. In their calculation, the PWE method was used by assuming an artificial transverse velocity in the air. All the mentioned works considered the case of the surface normal to the cylindrical scatterers. Manzanares-Martínez and Ramos-Mendieta[14] are the only ones who studied the case of the surface parallel to the cylinders. Some researchers aimed at studying the SAWs in phononic structures experimentally.[15–19] Among them, Torres *et al.*[15] experimentally observed surface modes in a Hg/Al composite sample; Every *et al.*[16] and Vines *et al.*[17,18] conducted experimental studies on the Scholte-type SAWs generated by line-focus acoustic lens at the water-loaded surface of a 1D or 2D phononic crystal; and Meseguer *et al.*[19] reported experiments on the absolute band gaps for the SAWs in a marble quarry with drilled holes. Besides the above-mentioned works, we also notice that there is an increasing interest in SAWs in piezoelectric phononic crystals recently.[20–23]

We may notice that most theoretical computations for SAWs were performed by using the PWE method. However, as noted by Sun *et al.*[9] and Tanaka *et al.*,[10] the PWE method is not applicable to a phononic lattice with large acoustic mismatch and therefore other method, e.g., FDTD method,[9,10] which cannot yield spectra directly, has to be employed. Furthermore, when the PWE method is used for an air/solid system, one has to assume an artificial transverse velocity in the air.[11–13] In this regard, we argue that an improved method should be developed for computing the band structures of SAWs in various phononic crystals including the one with large acoustic mismatch and the mixed fluid/solid system. Recently the present authors[24] have developed

a different method based on wavelets, which was proved successful in band-gap calculation of all kinds of 2D phononic crystals for BAWs. Here in this paper, we will extend the wavelet method[24] to SAWs. The outline of the paper is as follows: the wavelet algorithm is described in Sec. II; the numerical results are presented in Sec. III and then followed by a summary in Sec. IV.

II. WAVELET METHOD FOR SURFACE WAVES IN A 2D PHONONIC CRYSTAL

We assume the system to be an elastic continuum composed of a periodic array of cylinders of material A embedded in a background material B. In the inhomogeneous linear elastic anisotropic medium without body forces, the equation governing the motion for harmonic plane waves can be written as

$$-\rho(\mathbf{x})\omega^2\mathbf{u}(\mathbf{r}) = \nabla \cdot [\mathbb{C}(\mathbf{x}):\nabla\mathbf{u}(\mathbf{r})], \qquad (1)$$

where $\mathbf{u}(\mathbf{r})$ is the displacement vector; $\mathbf{r}=(\mathbf{x},z)=(x,y,z)$ is the position vector; $\nabla=(\frac{\partial}{\partial x}, \frac{\partial}{\partial y}, \frac{\partial}{\partial z})$ is a 3D nabla; ":" denotes double dot product; ω is the circular frequency; and $\rho(\mathbf{x})$ and $\mathbb{C}(\mathbf{x})$ are the position-dependent mass density and elastic stiffness tensor, respectively, which describe the properties of the materials. For isotropic materials, the components of $\mathbb{C}(\mathbf{x})$ are $C_{ijkl}=\lambda(\mathbf{x})\delta_{ij}\delta_{kl}+\mu(\mathbf{x})(\delta_{ik}\delta_{jl}+\delta_{il}\delta_{jk})$ where $\lambda(\mathbf{x})$ is Lamé constant and $\mu(\mathbf{x})$ is shear modulus. Then the longitudinal and transverse-wave speeds are given by $c_l = \sqrt{(\lambda+2\mu)/\rho}$ and $c_t=\sqrt{\mu/\rho}$. For fluid $\mu=0$ and no transverse mode exists. We take the z axis parallel to the cylinders and perpendicular to the free surface ($x-y$ plane). The phononic crystal occupies the halfspace of $z>0$. The system is assumed to be periodic in the $x-y$ plane. In utilizing the Bloch theorem, the displacement vector $\mathbf{u}(\mathbf{r})$ may be written as

$$\mathbf{u}(\mathbf{r}) = e^{i(\mathbf{k}\cdot\mathbf{r})}\mathbf{u}_\mathbf{k}(\mathbf{x}), \qquad (2)$$

where $\mathbf{u}_\mathbf{k}(\mathbf{x})$ is two-dimensional and periodic and $\mathbf{k}=(k_x,k_y,k_z)$ is a 3D wave vector. Both $\mathbf{u}_\mathbf{k}(\mathbf{x})$ and $\mathbf{k}$ are defined in the first Brillouin zone (BZ) of the lattice. Substituting Eq. (2) into Eq. (1), we obtain

$$(\nabla + i\mathbf{k}) \cdot [\mathbb{C}:(\nabla + i\mathbf{k}) \otimes \mathbf{u}_\mathbf{k}(\mathbf{x})] = -\rho(\mathbf{x})\omega^2\mathbf{u}_\mathbf{k}(\mathbf{x}), \qquad (3)$$

which can be rewritten in a variational form as

$$\langle v,(\nabla + i\mathbf{k}) \cdot [\mathbb{C}:(\nabla + i\mathbf{k}) \otimes \mathbf{u}_\mathbf{k}(\mathbf{x})]\rangle$$
$$= -\omega^2\langle v,\rho(\mathbf{x})\mathbf{u}_\mathbf{k}(\mathbf{x})\rangle, \quad \forall\, v \in L^2(\Omega), \qquad (4)$$

or equivalently in the integral form

$$\int_\Omega \mathbb{C}:(\nabla + i\mathbf{k}) \otimes \mathbf{u}_\mathbf{k}(\mathbf{x}) \cdot \overline{(\nabla + i\mathbf{k})v}\,d\mathbf{r} = \omega^2\int_\Omega \rho(\mathbf{x})\mathbf{u}_\mathbf{k}(\mathbf{x})\bar{v}\,d\mathbf{r}, \qquad (5)$$

where v is an arbitrary square-integrable function. Due to the spatial periodicity, $\mathbf{u}_\mathbf{k}(\mathbf{x})$ and the material constants can be expanded in periodic wavelets.[24] As in Ref. 24, we will use the periodic Haar wavelet basis to represent the discontinuous functions of the density $\rho(\mathbf{x})$ and elastic stiffness tensor

$\mathbb{C}(\mathbf{x})$ and use the periodic Bior 3.9 wavelet basis for the displacement fields $\mathbf{u}_\mathbf{k}(\mathbf{x})$. The wavelet expansions of these functions are denoted as

$$\mathbf{u}_\mathbf{k}(\mathbf{x}) = \sum_{b_m \in \Psi_{j_0,J}} \hat{\mathbf{u}}_{\mathbf{k},m}b_m, \qquad (6)$$

$$\alpha(\mathbf{x}) = \sum_{d_m \in \Psi_{j_0,J}} \hat{\alpha}_{\mathbf{k},m}d_m, \qquad (7)$$

where $\alpha(\mathbf{x})=[\rho(\mathbf{x}),\mathbb{C}(\mathbf{x})]$; $\hat{\alpha}_{\mathbf{k},m}$ and $\hat{\mathbf{u}}_{\mathbf{k},m}$ are the corresponding wavelet coefficients; and the localized basis set $\Psi_{j_0,J}$ is

$$\{\varphi^{\text{period}}_{j_0,k1,k2}\!:\!k1 = 0, \ldots, 2^{j_0} - 1; k2 = 0, \ldots, 2^{j_0} - 1\}$$
$$\cup \{\psi^{(\gamma),\text{period}}_{j,k1,k2}\!:\!\gamma = 1,2,3; k1 = 0, \ldots, 2^j - 1;$$
$$k2 = 0, \ldots, 2^j - 1; j = j_0, \ldots, J - 1\}. \qquad (8)$$

Each function in this set is 2D periodic wavelets and scaling functions consisting of a product of two 1D periodic wavelets and scaling functions.[24] The integer J fixes the approximation degree as well as the maximum number 2^{2J} of the wavelets and scaling basis functions used in the expansion. An adaptive algorithm would add or remove wavelets during calculations without restriction on the integer J and would stop when a desired accuracy is obtained. For details, we refer to Ref. 24.

Substituting Eq. (6) into Eq. (5) and then choosing the arbitrary square-integrable function $v=b_q$, we obtain

$$\int_\Omega \mathbb{C}:[(\nabla + i\mathbf{k}) \otimes \hat{\mathbf{u}}_\mathbf{k}b_p] \cdot \overline{(\nabla + i\mathbf{k})\tilde{b}_q}\,d\mathbf{r} = \omega^2\int_\Omega \rho(\mathbf{x})\hat{\mathbf{u}}_\mathbf{k}b_p\tilde{b}_q\,d\mathbf{r}, \qquad (9)$$

which may be rewritten in a compact form

$$\mathbf{A}_\mathbf{k}\mathbf{W}_\mathbf{k} = \omega^2\mathbf{B}_\mathbf{k}\mathbf{W}_\mathbf{k}, \qquad (10)$$

where $\mathbf{W}_\mathbf{k}$ is a column vector containing $\hat{u}_{x\mathbf{k}}$, $\hat{u}_{y\mathbf{k}}$, and $\hat{u}_{z\mathbf{k}}$; and $\mathbf{A}_\mathbf{k}$ and $\mathbf{B}_\mathbf{k}$ are large sparse matrices with their elements given by

$$(\mathbf{A}_\mathbf{k})_{p,q} = \int_\Omega \mathbb{C}:[(\nabla + i\mathbf{k})b_p] \cdot \overline{(\nabla + i\mathbf{k})\tilde{b}_q}\,d\mathbf{r}, \qquad (11)$$

$$(\mathbf{B}_\mathbf{k})_{p,q} = \int_\Omega \rho(\mathbf{x})b_p\tilde{b}_q\,d\mathbf{r}. \qquad (12)$$

In Eqs. (9)–(12), "$\sim$" implies the dual basis functions. If the BAWs are considered, the frequencies can be obtained by solving the eigenvalue equation (10). We have presented detailed analysis and computation in Ref. 24 for the BAWs with $k_z=0$. But here in this paper, we are looking for the SAW solutions; therefore, we should further consider the boundary conditions at the surface $z=0$,

$$\boldsymbol{\sigma} \cdot \mathbf{n}|_{z=0} = (\mathbb{C}:\nabla\mathbf{u}) \cdot \mathbf{n}|_{z=0} = \mathbf{0}, \qquad (13)$$

where the surface is assumed to be stress free; $\boldsymbol{\sigma}$ and $\mathbf{n}$ are the stress tensor and the unit normal vector of the surface.

The displacement field for the SAW [Eq. (6)] can be rewritten as

$$\mathbf{u}(\mathbf{r}) = \sum_{b_m \in \Psi_{j_0, J}} e^{i(\mathbf{k}_\parallel \cdot \mathbf{x})} \sum_l \hat{\mathbf{u}}_{\mathbf{k}, m}^{(l)} e^{i k_z^{(l)} z} b_m, \qquad (14)$$

where $\mathbf{k}_\parallel = (k_x, k_y)$. Substituting Eq. (14) into Eq. (13), we have

$$\sum_{b \in \Psi_{j_0, J}} \sum_l \{\mathbb{C} : [(\nabla + i\mathbf{k}^{(l)}) \otimes \hat{\mathbf{u}}_{\mathbf{k}}^{(l)} b_m] \cdot \mathbf{n} + \mathbb{C} : [\nabla b_m \otimes \hat{\mathbf{u}}_{\mathbf{k}}^{(l)}] \cdot \mathbf{n}\}$$

$$= \mathbf{0}, \qquad (15)$$

which may be rewritten in an integral form

$$\sum_{b \in \Psi_{j_0, J}} \sum_l \int_\Omega \{[\mathbb{C} : \{[\nabla + i\mathbf{k}^{(l)}] \otimes \hat{\mathbf{u}}_{\mathbf{k}}^{(l)} b_p\} \cdot \mathbf{n}] \tilde{b}_q$$

$$+ \{\mathbb{C} : [\nabla b_p \otimes \hat{\mathbf{u}}_{\mathbf{k}}^{(l)}] \cdot \mathbf{n}\} \tilde{b}_q\} = \mathbf{0}, \qquad (16)$$

where $\mathbf{k}^{(l)} = (\mathbf{k}_\parallel, k_z^{(l)})$. This leads to the linear equations for $\hat{\mathbf{u}}_{\mathbf{k}}^{(l)}$,

$$\tilde{\mathbf{H}} \hat{\mathbf{u}}_{\mathbf{k}} = 0, \qquad (17)$$

where the expression of $\tilde{\mathbf{H}}$ may be obtained from Eq. (16) and will not be given here.

The eigenfrequency and the complex wave number k_z (governing the localization of the wave near the surface) of the SAW mode could be obtained by solving Eqs. (9) and (17) simultaneously, which however is a nontrivial task. Here we will use the method of Tanaka and Tamura[5] to find the solutions of the eigenfrequency and k_z for a given $\mathbf{k}_\parallel$. First we solve $k_z^{(l)}$ from Eq. (9) for a given circular frequency ω, then calculate the normalized boundary-condition determinant $|\det(\tilde{\mathbf{H}})| / |\det(\tilde{\mathbf{H}})|_{\max}$ and plot it as a function of the frequency ω. According to the exponential dependence of z in Eq. (2), the real part of $k_z^{(l)}$ denotes the plane-wave propagation in the z direction, and a positive nonvanishing imaginary part represents attenuation in the z direction. If the wave vector $\mathbf{k}_\parallel$ parallel to the surface is real and all $k_z^{(l)}$ ($l = 1 - 3 \times 2^{2J}$) have positive imaginary parts, the deep minimum of the curve $|\det(\tilde{\mathbf{H}})| / |\det(\tilde{\mathbf{H}})|_{\max} \sim \omega$ corresponds to the so-called "pure" SAW (generally we omit the word "pure" in this paper except when it is emphasized); if the wave vector $\mathbf{k}_\parallel$ is expanded into a complex number $\mathbf{k}_\parallel (1 + i\varepsilon)$ with the positive number ε having the magnitude of 1×10^{-2} or less and some of $k_z^{(l)}$ have negative imaginary parts, the deep minimum of the curve represents a PSAW. For details of the above procedure, we refer to Ref. 5.

In calculation, we first compute $|\det(\tilde{\mathbf{H}})| / |\det(\tilde{\mathbf{H}})|_{\max}$ versus the frequency ω by taking $\varepsilon = 0$ for a given $\mathbf{k}_\parallel$. If we find its value is less than 1×10^{-4} at a particular frequency, we introduce the decay parameter ε and try its magnitude (near 1×10^{-2} or less) to compute $|\det(\tilde{\mathbf{H}})| / |\det(\tilde{\mathbf{H}})|_{\max}$ until $|\det(\tilde{\mathbf{H}})| / |\det(\tilde{\mathbf{H}})|_{\max} < 10^{-10}$ is satisfied. Then we say that this value contributes a minimum to a PSAW.

TABLE I. The elastic properties of the materials utilized in the examples.

Material	Density (kg/m³)	Elastic constants (1×10^{10} N/m²)	
		λ	μ
Al	2695	6.1	2.5
Ni	8905	16.4	8
W	19300	19.74	15.13
Si	2330	5.27	6.7
Steel	7890	10	8.18
Gold	19500	16.03	2.99
Polymer	1350	1.4	0.8
Epoxy	1180	0.442	0.158

III. NUMERICAL EXAMPLES AND DISCUSSION

In this section, numerical results will be presented for several typical phononic structures including solid/solid systems and mixed fluid/solid systems with or without defects. These lattices consist of cylinders (A) embedded in a background material (B) forming square or triangular lattices with lattice spacing a. To characterize the acoustic mismatch of the systems, we define two acoustic impendence ratios, Z_A^L / Z_B^L and Z_A^T / Z_B^T, where $Z^L = \rho c_l$ and $Z^T = \rho c_t$. The elastic properties of the materials utilized in the calculation are listed in Table I. We compute not only the samples already studied in literatures to validate the present method but also some new samples to show more properties of SAWs and PSAWs. In Figs. 1 and 6–15 illustrating the dispersion curves, the solid lines are for the mixed BAWs, the dashed lines for the purely transverse BAWs, the solid circles for the SAW modes, and the open circles for the PSAW modes. The frequency ω is normalized by $a/c_{t,\text{base}}$ where $c_{t,\text{base}}$ is the transverse-wave velocity of the background material.

A. Fluid/solid systems

In Ref. 11, the dispersion relations of the surface and bulk modes in a square lattice of air/silicon with air filling fraction $f = 0.283$ were reported; the PWE method was used with assuming an artificial transverse velocity in the air. For comparison, we recompute their sample with $f = 0.28$. Shown in Fig. 1(a) are the dispersion curves produced from the present method by taking 1024 wavelets. One may find that the present result is in agreement with that in Ref. 11 where the detailed discussion of BAWs and SAWs was presented. In our method, no artificial transverse velocity in the air is assumed. For comparison, we also calculate the band structures of air/aluminum system with the same filling fraction; see Fig. 1(b). Almost no difference can be observed between Figs. 1(a) and 1(b) although the background materials are different. We notice that the acoustic impedance ratios are so small $(Z_{\text{air}}^L / Z_{\text{Si}}^L = 1.63 \times 10^{-5}, Z_{\text{air}}^L / Z_{\text{Al}}^L = 1.96 \times 10^{-5})$ that the air may be ignored in both systems.

It is worth noting that the first SAW branch appears above the lowest BAW branch along most part of boundary of the irreducible Brillouin zone especially along the highly sym-
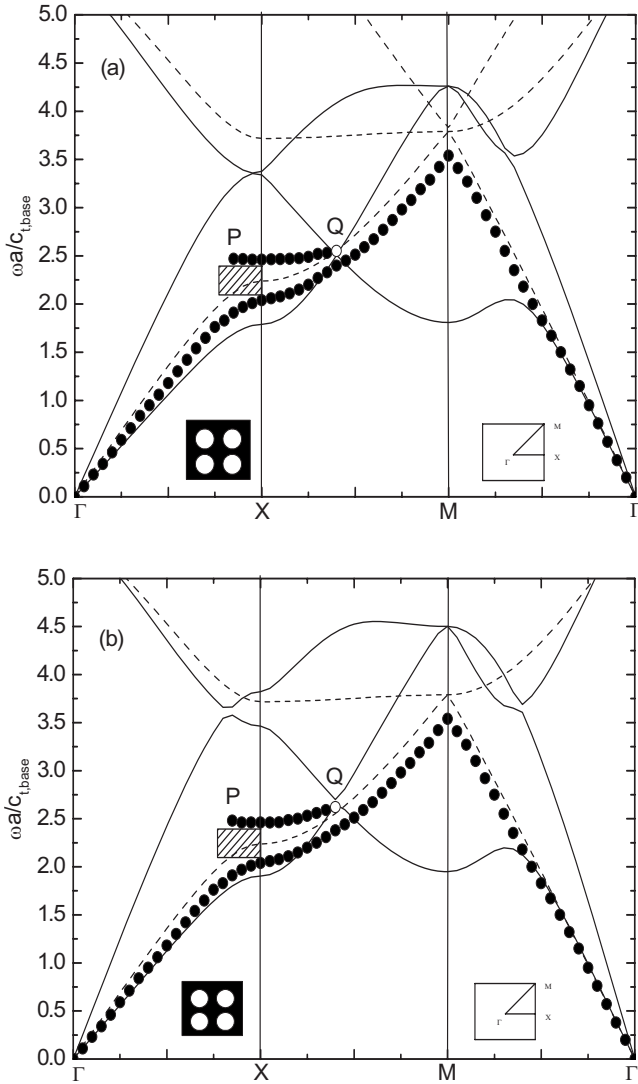
FIG. 1. Dispersion curves of BAW and SAW modes in square lattices of air-filled circular holes in a (a) silicon host and (b) an aluminum host. A SAW-SAW gap appears at point X. The higher SAW mode ceased approximately at point Q where the sharp bend of the bulk mode occurs.

metric directions $\Gamma-X$ and $\Gamma-M$; It is also the case in Refs. 11 and 13. Calculations show that these surface modes are indeed the "pure" SAWs. As an illustration, Fig. 2 plots the curve of $|\det(\widetilde{\mathbf{H}})|/|\det(\widetilde{\mathbf{H}})|_{max}$ with $\varepsilon=0$ versus the frequency for the point X of Fig. 1(a). Two deep minima appear at $\omega a/c_{t,\text{base}}=2.04$ and 2.46, which correspond to two "pure" SAW modes. One may also notice that the first SAW branch follows the purely transverse BAW branch (the dashed lines) just below it along the whole boundary of the irreducible Brillouin zone. Therefore, we infer that the SAW modes should be closely related to this BAW branch instead of the lowest BAW branch. Indeed, along the highly symmetric directions the lowest BAW branch is a pure shear mode with the horizontal polarization; but the SAWs are polarized in the sagittal plane and thus are completely decoupled from this bulk mode.[5] The above-mentioned behavior is universal for all systems with fluid scatterers embedded in a solid host; see also Figs. 6–8.
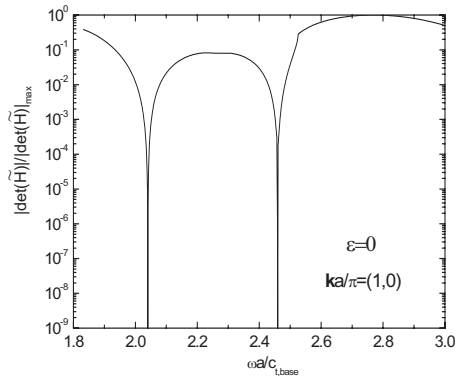
FIG. 2. The normalized magnitude of the boundary-condition determinant $|\det(\widetilde{\mathbf{H}})|$ with $\varepsilon=0$ vs frequency at point X shown in Fig. 1(a). Two deep minima are found at $\omega a/c_{t,\text{base}}=2.04$ and 2.46, which correspond to the SAW modes propagating parallel to the interface.

Another interesting phenomenon is that the upper SAW branch (the folded one) extends from point X to the left vanishing at points P and to the right vanishing at points Q (it is also the case in Refs. 11 and 13). The similar phenomenon can be seen in Fig. 1(b) as well as in Figs. 6 and 8 (in Fig. 8, SAW other than PSAW appears at point Q). It is noted that point Q is the crosspoint of all BAW branches. Therefore stop of the SAW branch at point Q might be owing to the mode transformation at this point. However the physical origin of this feature at point P is still not clear. Here we show why this happens at both points Q and P from mathematics. Figure 3(a) displays the curve of $|\det(\widetilde{\mathbf{H}})|/|\det(\widetilde{\mathbf{H}})_{max}|$ for ε
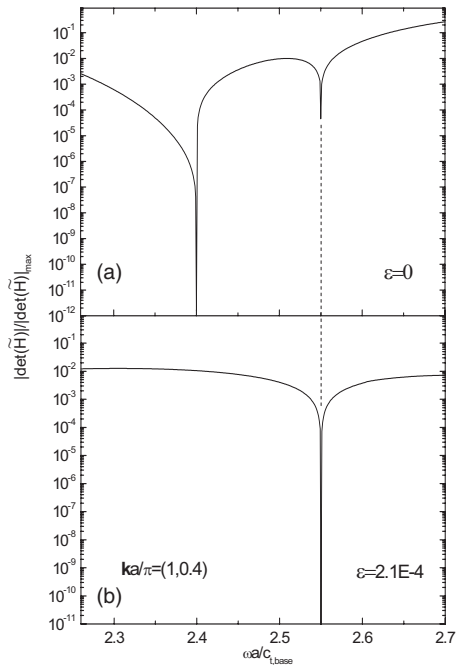
FIG. 3. The normalized magnitude of the boundary-condition determinant $|\det(\widetilde{\mathbf{H}})|$ vs frequency at point Q shown in Fig. 1(a); (a) for the SAW mode with $\varepsilon=0$ at $\omega a/c_{t,\text{base}}=2.40$ and (b) for the PSAW mode with $\varepsilon=2.1\times10^{-4}$ at $\omega a/c_{t,\text{base}}=2.55$.
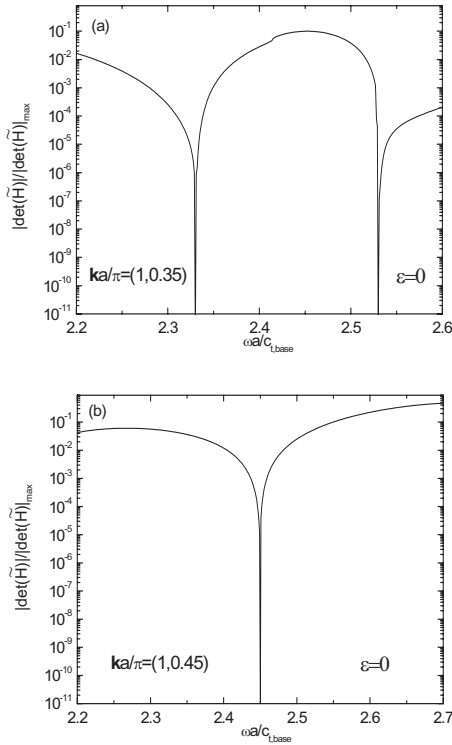
FIG. 4. The normalized magnitude of the boundary-condition determinant $|\det(\widetilde{\mathbf{H}})|$ vs frequency at (a) left and (b) right of point Q shown in Fig. 1(a). Two deep minima with $\varepsilon=0$ at $\omega a/c_{t,\text{base}}$ =2.33 and 2.53 corresponding to the SAW modes are shown in (a), and one deep minimum with $\varepsilon=0$ at $\omega a/c_{t,\text{base}}=2.45$ in (b). No PSAW modes are found.

=0 versus the frequency for point Q of Fig. 1(a). A deep minimum appears at $\omega a/c_{t,\text{base}}=2.40$ corresponding to a SAW mode. A local minimum is shown at $\omega a/c_{t,\text{base}}=2.55$, which will develop a deep minimum corresponding to a PSAW mode when a small value (2.1×10^{-4}) of ε is given [see Fig. 3(b)]. We also calculate $|\det(\widetilde{\mathbf{H}})|/|\det(\widetilde{\mathbf{H}})_{\text{max}}|$ with $\varepsilon=0$ at the left and right of point Q and illustrate the curves in Figs. 4(a) and 4(b), respectively. At the left of point Q, two deep minima appear at $\omega a/c_{t,\text{base}}=2.33$ and 2.53, which represent two SAW modes, see Fig. 4(a); while at the right of point Q [Fig. 4(b)], only one deep minimum is shown at $\omega a/c_{t,\text{base}}=2.45$, that is, the upper SAW branch disappears beyond point Q. Neither can we find PSAW modes beyond points Q through the detailed calculations. At point P, two deep minima of $|\det(\widetilde{\mathbf{H}})|/|\det(\widetilde{\mathbf{H}})_{\text{max}}|\sim\omega$ curve with $\varepsilon=0$ are shown at $\omega a/c_{t,\text{base}}=1.91$ and 2.47 corresponding to two SAW modes; see Fig. 5(a). But beyond point P we find neither a SAW nor a PSAW mode. For instance, Fig. 5(b) illustrates the $|\det(\widetilde{\mathbf{H}})|/|\det(\widetilde{\mathbf{H}})_{\text{max}}|\sim\omega$ curve with $\varepsilon=0$ at the left of point P. Two minima with values less than 1×10^{-3} appear at $\omega a/c_{t,\text{base}}=2.65$ and 2.77. These do not contribute to SAWs. We then give positive values to ε to show how deep these two minima can go; see the inset of Fig. 5(b). It is shown that the minimum at point A almost does go deeper while that the minimum at B goes to 2.33×10^{-6} near ε =0.01. According to the criterion to define a PSAW as discussed at the end of Sec. II, these two minima do not con-
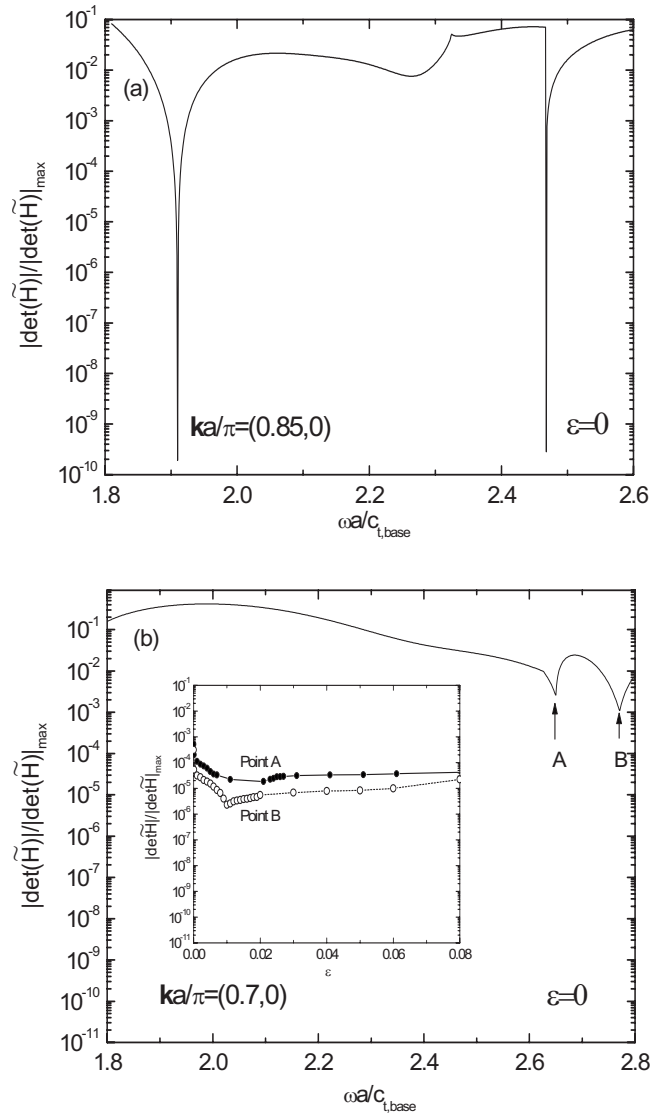
FIG. 5. The normalized magnitude of the boundary-condition determinant $|\det(\widetilde{\mathbf{H}})|$ vs frequency at (a) point P and (b) its left shown in Fig. 1(a). Two deep minima with $\varepsilon=0$ at $\omega a/c_{t,\text{base}}$ =1.91 and 2.47 corresponding to the SAW modes are shown in (a); no deep minima contributing to SAW and PSAW modes are shown in (b).

tribute to PSAWs. Therefore neither a SAW nor a PSAW appears beyond point P.

To examine the influence of the scatterer shape and lattice structure on the BAW and SAW dispersion relations, we illustrate the dispersion curves for the air/silicon system with square scatterers in a square lattice (Fig. 6) and with circle scatterers in a triangle lattice (Fig. 7). The same filling fraction as in Fig. 1 is chosen. Almost no difference can be observed between the dispersion curves of SAWs for circular scatterers [Fig. 1(a)] and square scatterers (Fig. 6); although the dispersion curves of BAWs for these two cases show observable difference near point M. If we compare Figs. 1(a) and 7, we may find distinguishing difference between the curves in these two figures. PSAW modes are shown near point M in the triangle structures and no SAW band gap
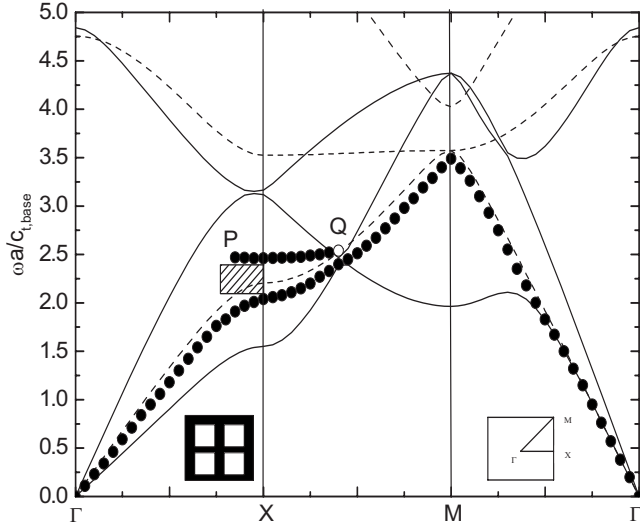
FIG. 6. Dispersion curves of BAW and SAW modes in a square lattice of air-filled square holes in a silicon host. A SAW-SAW gap appears at point X. The higher SAW mode ceased approximately at point Q where the sharp bend of the bulk mode occurs.

appears at point X (Fig. 7). Therefore we could say that the scatterer shape has little influence but the lattice structure has significant influence on the band structures for the surface wave modes.

Next we compute the dispersion curves of SAWs for a liquid/solid phononic crystal consisting of a square lattice of water-filled holes in an aluminum host ($Z^L_{water}/Z^L_{Al}=0.086$) with the same filling fraction as before. The results are shown in Fig. 8. Since the PWE method fails to liquid/solid systems, no band structures of SAWs were reported until now. A comparison of Fig. 8 to Fig. 1(b) shows the difference between the air/Al and water/Al systems: The dispersion curves of the two systems are different for BAWs (especially at higher frequencies) but similar for SAWs—the

FIG. 7. Dispersion curves of BAW and SAW modes in a triangular lattice of air-filled circular holes in silicon host. No SAW-SAW gap appears at point X. The folded surface wave branch is found at point M.
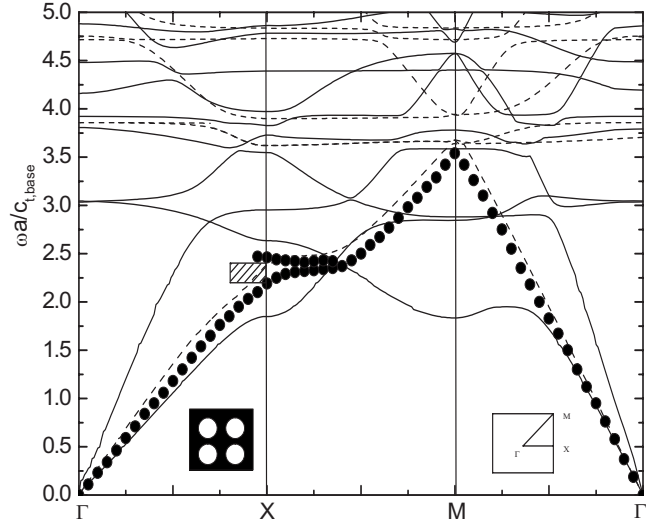
FIG. 8. Dispersion curves of BAW and SAW modes in a square lattice of water-filled circular holes in an aluminum host. A SAW-SAW gap appears at point X. Along the X-M direction, the higher and lower SAW branches approach where the sharp bend of the bulk mode occurs.

two SAW branches near point X are a little closer in water/Al than in air/Al.

The numerical examples in this section show that the present method can yield accurate results of band structures for surface modes in fluid/solid phononic crystals with circular or square scatterers and square or triangle lattices. The advantage of the present method is that no assumption of an artificial transverse velocity in the air is necessary and that the method does work well in liquid/solid systems for which the PWE method fails.

B. Solid/solid systems with small acoustic mismatch

The PWE method can yield accurate numerical results for the surface modes of the solid phononic crystals with small acoustic mismatch (Z^L_A/Z^L_B and Z^T_A/Z^T_B smaller than one), which were extensively studied by Wu *et al.*[8] They considered four typical systems: Al/Ni, AlAs/GaAs, Al/ZnO, and Al/Ba$_2$NaNb$_5$O$_{15}$. The background materials in the last three cases are anisotropic solids with their material constants given in Ref. 8. Here we recompute the Al/Ni ($Z^L_{Al}/Z^L_{Ni}=0.32, Z^T_{Al}/Z^T_{Ni}=0.31$) and Al/Ba$_2$NaNb$_5O_{15}$ ($Z^L_{Al}/Z^L_{Ba}=0.50, Z^T_{Al}/Z^T_{Ba}=0.44$) square lattices as a check of our method. The band structures with filling fraction $f=0.6$ for both bulk and surface modes are plotted in Fig. 9. It is seen that the present results are in good agreement with those shown in Figs. 7 and 12 of Ref. 8. Detailed properties of the surface modes in such systems were discussed in Ref. 8. Here we would just mention that the SAW-SAW gap at point X and PSAW-PSAW gap at point M decrease as the acoustic impendence ratio increases to one because the heterogeneous medium becomes more even. Next we will show the properties of the surface modes in solid/solid systems with moderate and large acoustic mismatch (Z^L_A/Z^L_B and Z^T_A/Z^T_B bigger than one).
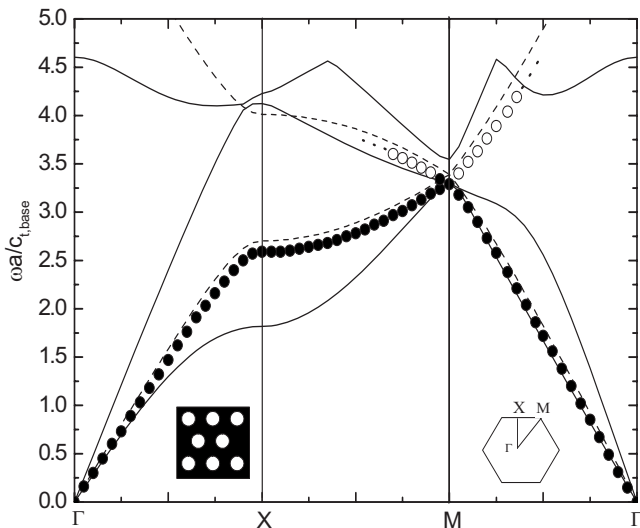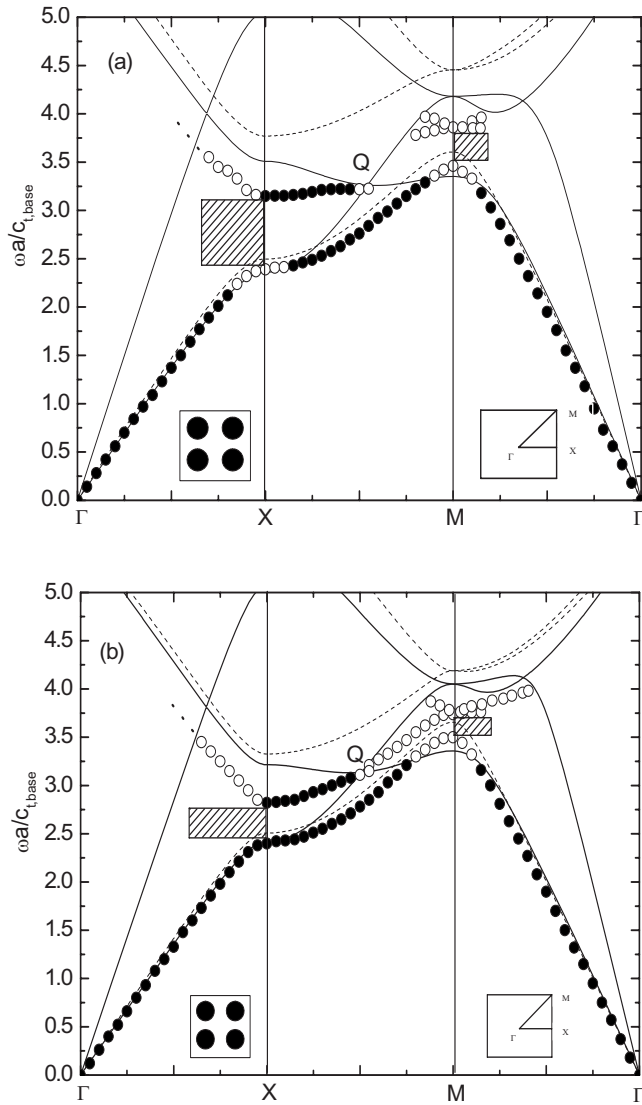
FIG. 9. Dispersion curves of BAW and SAW modes in square lattices of aluminum cylinders in a (a) nickel host and a (b) barium sodium niobate host. A SAW-SAW gap appears at point X and a PSAW-PSAW gap at point M. The higher SAW mode ceases approximately at point Q where the sharp bend of the bulk mode occurs.

The transformation from the SAWs to PSAWs and visa versa in the lowest branches of the surface modes can be observed in Fig. 9. This happens when the branches surpass the lowest BAW branches, in which case the surface wave speed is lower than that of the slowest bulk wave. To see the details, we illustrate in Fig. 10(a) the magnification of the dispersion relations along $\Gamma - X$ direction of Fig. 9(a). Before point A (marked with a cross symbol), the surface mode appears as "pure" SAWs (the solid circles) below the lowest BAW branch. Then after point A, the surface mode surpasses the lowest BAW branch changing from SAWs to PSAWs. This behavior is also demonstrated by the $k_x - k_z$ section of the constant-frequency surfaces of the bulk waves; see Fig. 10(b). For a given frequency a little higher than point A, the wave number k_{PSW} of the surface mode is smaller than that of the slowest bulk mode k_{ST}. Then we can find a real wave
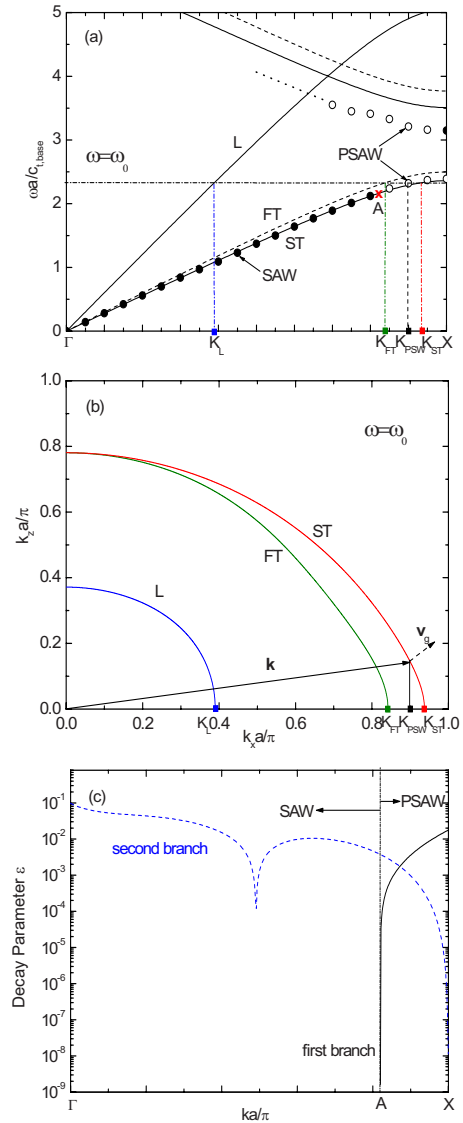
FIG. 10. (Color online) (a) Magnification of the dispersion relations along the $\Gamma - X$ direction of Fig. 9(a). The points k_L, k_{FT}, k_{ST}, and k_{PSW} indicate the wave numbers in $x-y$ plane of the bulk and surface waves of a given frequency ω_0. (b) The section of the constant-frequency ($\omega = \omega_0$) surfaces of the bulk waves by the $k_x - k_z$ plane corresponding to (a). A real wave vector **k** with its component parallel to the surface equal to k_{PSW} is shown; and the corresponding group-velocity v_g points inside the substrate ($z > 0$). (c) Decay parameter of the PSAW modes along the $\Gamma - X$ direction of (a). The solid curve shows the result for the first branch. ε decreases as the wave vector **k** varies from point X to point A and vanishes at point A where the wave mode transforms from PSAW into SAW. The dashed line corresponds to the second branch. ε vanishes at point X where the wave mode transforms from PSAW into SAW. A much small value of ε appears at $ka/\pi = 0.49$.

vector **k** with its component parallel to the surface equal to k_{PSW} and the corresponding group-velocity v_g points inside the substrate ($z > 0$). This means that if the surface wave couples to the bulk mode, it will attenuate by radiating acoustic energy into the bulk of the system leading to PSAWs. Decay parameters of the PSAW modes along the $\Gamma - X$ direction are plotted in Fig. 10(c) for both the lowest
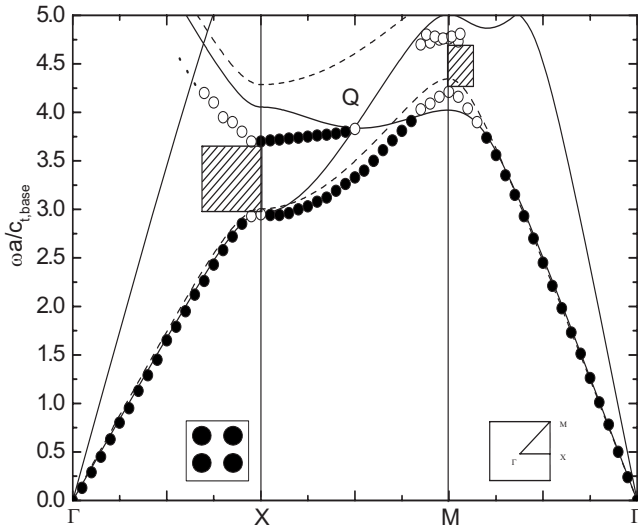
FIG. 11. Dispersion curves of BAW and SAW modes in square lattices of aluminum cylinders in a polymer host. A SAW-SAW gap appears at point X and a PSAW-PSAW gap at point M. The higher SAW mode ceases approximately at point Q where the sharp bend of the bulk mode occurs.

(solid line) and upper (dashed line) surface mode branches. For the lowest branch, ε decreases as the wave vector **k** varies from point X to point A and vanishes at point A where the wave mode transforms from PSAW into SAW. This behavior, which is also shown in Figs. 11 and 12(b), has been explored in details by Tanaka and Tamura[5] for the AlAs/GaAs system.

C. Solid/solid systems with moderate and large acoustic mismatch

In this section, we consider two solid/solid systems with moderate acoustic mismatch: Al/polymer ($Z_{\text{Al}}^{L}/Z_{\text{polymer}}^{L}=2.7$, $Z_{\text{Al}}^{T}/Z_{\text{polymer}}^{T}=2.5$) and W/Si ($Z_{\text{W}}^{L}/Z_{\text{Si}}^{L}=4.71, Z_{\text{W}}^{T}/Z_{\text{Si}}^{T}=4.33$) and two with large acoustic mismatch: Steel/epoxy ($Z_{\text{steel}}^{L}/Z_{\text{epoxy}}^{L}=15.25, Z_{\text{steel}}^{T}/Z_{\text{epoxy}}^{T}=18.61$) and Au/epoxy ($Z_{\text{Au}}^{L}/Z_{\text{epoxy}}^{L}=21.9, Z_{\text{Au}}^{T}/Z_{\text{epoxy}}^{T}=17.7$). The results of band structures for both bulk and surface modes are shown in Figs. 11–13. For the Al/polymer square lattice with $f=0.6$, the band structures of the surface modes (Fig. 11) show the similar properties as in Fig. 9 for the Al/Ni and Al/Ba$_2$NaNb$_5$O$_{15}$ with small acoustic mismatch. Both SAW-SAW gap at point X and PSAW-PSAW gap at point M appear. However, with the successive increase in acoustic mismatch, the band structures exhibit more distinguishing characteristics. For the W/Si square lattice with $f=0.175$ [Fig. 12(a)], there exist absolute BAW band gaps where the PSAW branch appears, and the SAW branch appears below the lowest bulk mode. It is generally expected that in an absolute band gap the surface modes are pure SAW modes. However detailed computation shows that they are indeed the PSAW modes [see Fig. 12(c)], which shows the normalized magnitude of the boundary-condition determinant $|\det(\tilde{\mathbf{H}})|$ versus the frequency at point M in Fig. 12(a). Although the exact physical origin of this feature is now clear,
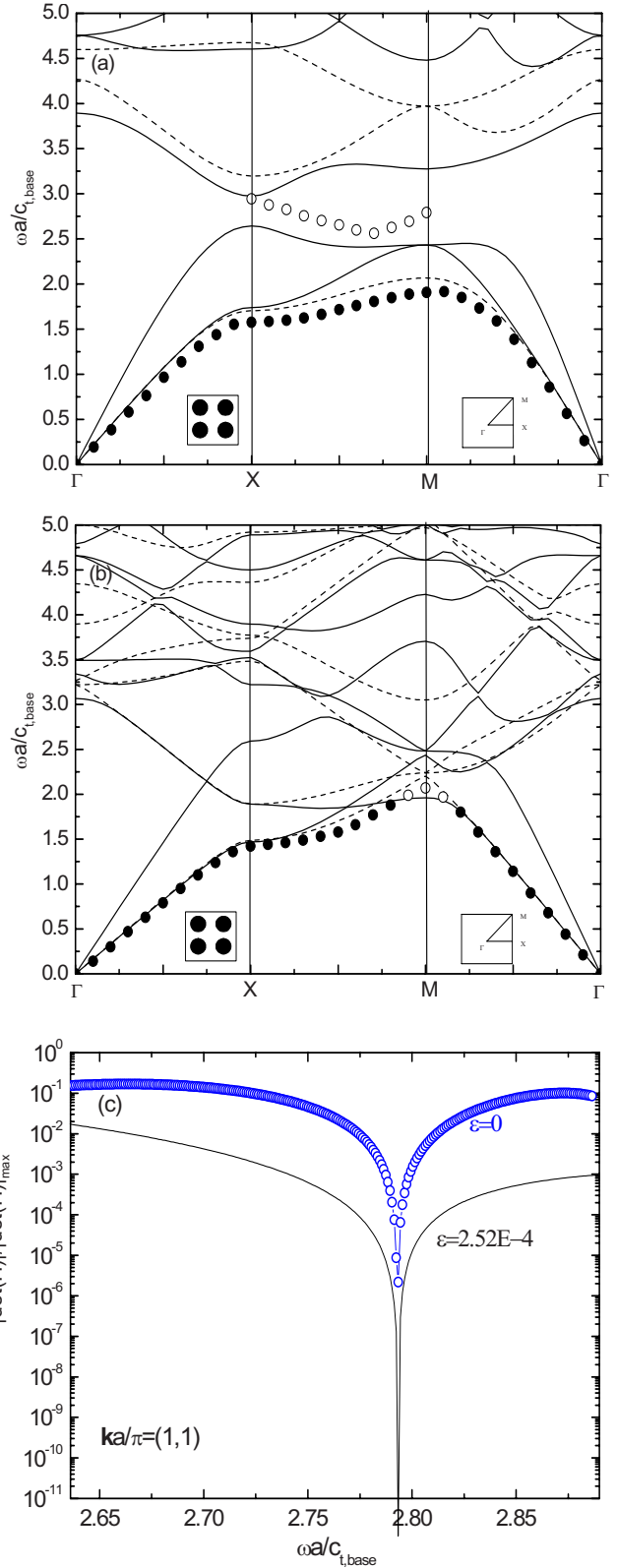
FIG. 12. (Color online) Dispersion curves of BAW and SAW modes in square lattices of tungsten cylinders in a silicon host with (a) $f=0.175$ and (b) $f=0.78$. (c) Normalized magnitude of the boundary-condition determinant $|\det(\tilde{\mathbf{H}})|$ vs frequency at point M in (a). A PSAW branch appears in the BAW gap in (a), but no similar PSAW branch appears in (b).
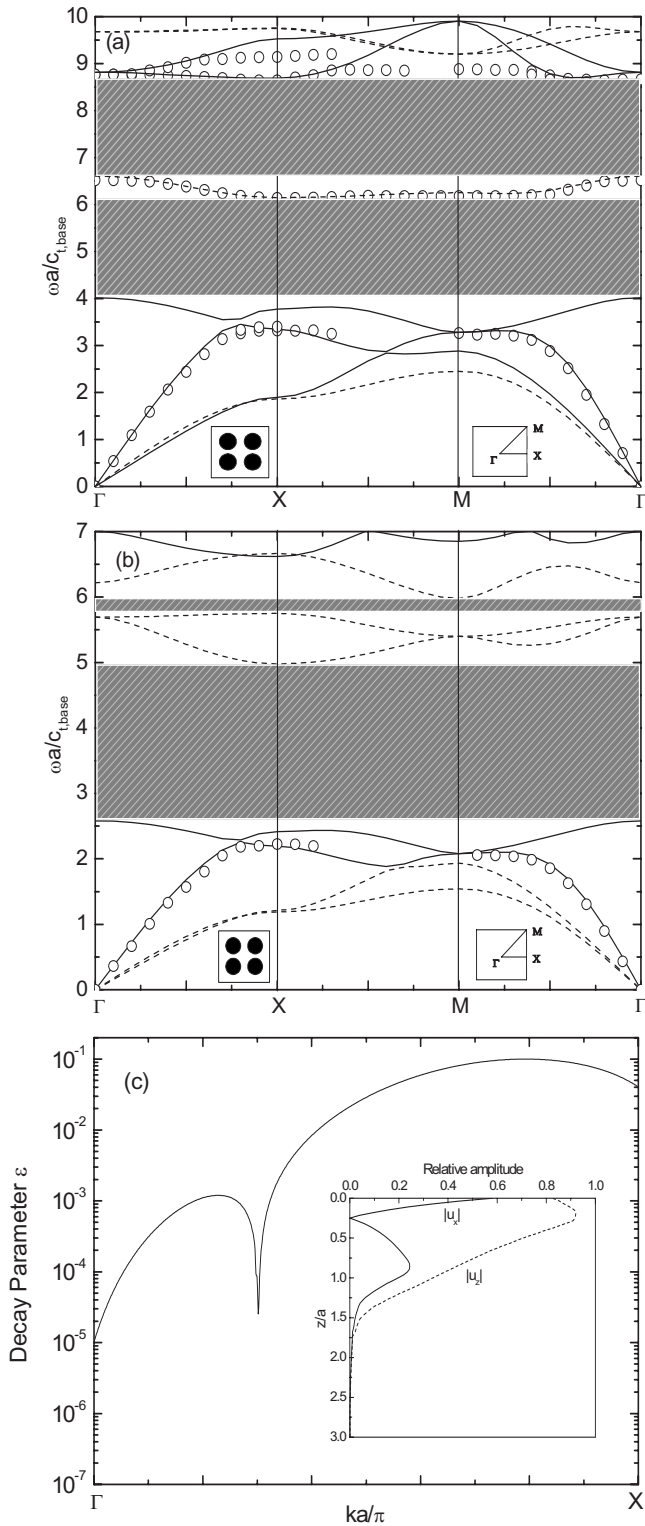
FIG. 13. Dispersion curves of BAW and SAW modes in square lattices of (a) steel cylinders and (b) gold cylinders in an epoxy host. Only PSAW modes exist. (c) Decay parameter of the PSAW modes along the $\Gamma-X$ direction of (b). ε increases as the wave vector **k** goes from point Γ to point X except near $ka/\pi=0.3$ where a much small value of ε appears. The inset of (c) shows the profile of the displacements at the center of the Au cylinder corresponding to the dip of ε appearing near $ka/\pi=0.3$.
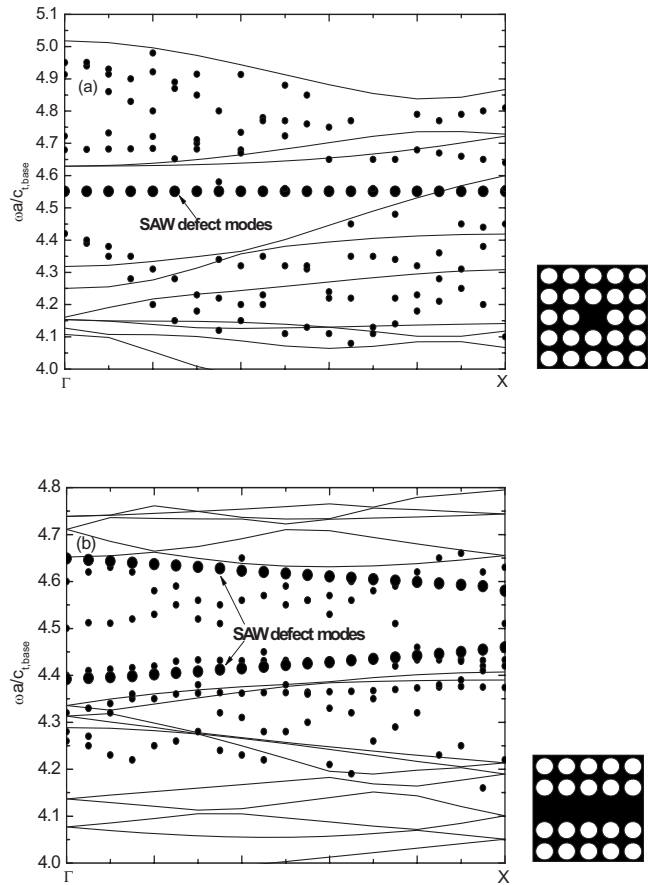
FIG. 14. Dispersion curves of BAW and SAW modes in square lattices of air-filled circular holes in silicon host with a (a) point and (b) line defect in a 5×5 supercell. The big solid circles represent the defect modes of the SAW. The small solid circles spread out are spurious roots.

one may attribute it to the larger acoustic mismatch of the system. The similar behavior is also exhibited in Fig. 15 for defected steel/epoxy system. When the filling fraction increases to $f=0.78$ [Fig. 12(b)], both absolute BAW band gap and PSAW branch disappear and the SAW degenerate to the
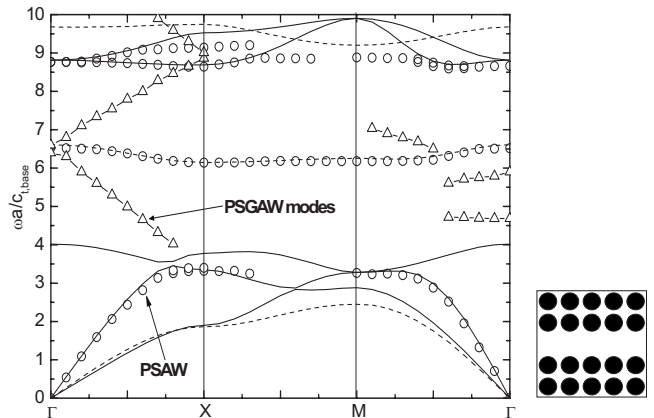
FIG. 15. Dispersion curves of BAW and SAW modes in a square lattice of steel cylinders in epoxy host with a line defect: a 5×5 supercell. The open triangles show the oblique bands of the PSGAW modes appearing in the BAW gaps.

PSAW near point M. This may imply that there exists a critical value of the filling fraction at which the SAW and PSAW will interchange.

For the steel/epoxy and Au/Epoxy square lattices with very large acoustic mismatch (Fig. 13), a PSAW branch appears near the first band of the longitudinal wave while no pure SAW exists. Decay parameter of the PSAW modes along the $\Gamma-X$ direction for the Au/Epoxy system is depicted in Fig. 13(c). ε increases as the wave vector **k** goes from point Γ to point X except near $ka/\pi=0.3$ where a much small value (about 1×10^{-4}) of ε appears. A small ε means that the PSAW is very stable. The inset of Fig. 13(c) shows the profile of the displacements at the center of the Au cylinder corresponding to the dip of ε appearing near ka/π $=0.3$. It is seen that the vibration is well localized near the surface (within one lattice constant a from the surface). For the steel/epoxy system, we can see the PSAW branches appearing at higher frequencies. It is noted that the PWE method encounters difficulties for systems with large acoustic mismatch. Tanaka *et al.*[9] and Sun and Wu[10] calculated the steel/epoxy square lattice using the FDTD method. The present results [Fig. 13(a)] are in basic agreement with Figs. 3(b) and 3(c) in Ref. 9 with a little difference at very high frequencies. Generally we could say that the present method is efficient for solid/solid phononic crystals with large acoustic mismatch.

D. Defect band structures for surface modes

Combined with the supercell technique, the present wavelet method can be used to study the defect states of the surface modes. Two systems, air/silicon and steel/epoxy square lattices are considered. A 5×5 supercell technique is employed and 4096 wavelets are included in wavelet expansions. Figure 14 illustrates the dispersion curves along Γ $-X$ of the air/silicon square lattice with a point or line defect ($f=0.61$). As the PWE method,[12] the wavelet method also yields scattered dots that represent the deep minima of the boundary-condition determinant. This is not strange because the main difference between these two methods is the basis functions used in series expansions. Since not all these roots represent the surface modes existing physically, we should separate the physical bands corresponding to the defect modes from the spurious roots. This can be done by selecting a row of continuous dots forming a straight line based on the physical features of the defect modes (it will be easier if much more points of **k** are calculated). Fortunately, we can indeed clearly see one flat band of the surface mode located in the point-defect region and two oblique bands (guided surface modes) in the line-defect region as shown by the big solid circles in Figs. 14(a) and 14(b), respectively. The spurious roots shown by the small solid circles are spread out.[12] The reason why the scattered roots appear is still an open problem. The point-defect states for the vacuum/silicon square lattice with $f=0.608$, a similar system as considered here, were calculated by Huang and Wu[12] (see Fig. 4 in Ref. 12), which is similar to Fig. 14(a).

At last, we compute the line-defect modes in the steel/epoxy system with large acoustic impedance, which was studied by Tanaka *et al.*[9] and Sun *et al.*[10] Shown in Fig. 15 are the results obtained with the present method. The pseudosurface guided acoustic wave (PSGAW) modes are shown by the open triangles. The present results are in good agreement with Fig. 6 of Ref. 9, which only gave the dispersion curves along $\Gamma-X$. It is noted that unlike Fig. 14, no scattered roots appear in Fig. 15. This difference may be due to the different material combinations of the two systems: Fig. 14 for the fluid/solid system and Fig. 15 for the solid/solid one.

IV. CONCLUDING REMARKS

The wavelet-based method developed in Ref. 24 to calculate the band structures of bulk waves in 2D phononic crystals is extended to surface wave modes. Both mixed fluid/solid and solid/solid systems with small or large acoustic mismatch were considered. The defect modes of the surface waves are also calculated by using the supercell technique. The method is validated by recomputing the samples already studied in literatures. The results show some merits of the present method. For instance, the method can yield accurate results of band structures for surface modes in air/solid systems without assuming an artificial transverse velocity in the air; it is efficient for liquid/solid systems and solid/solid systems with large acoustic mismatch for which the PWE method fails. The present method may serve as an alternative method for studying surface waves in general phononic lattices.

In addition, we also apply the present method to some new samples to show more properties of the surface modes. The influences of various factors, especially the acoustic mismatch, on the surface modes are discussed in detail. It is found that the acoustic mismatch plays an important role in the propagation of surface modes. For the cases with the acoustic impendence ratios far smaller than one, e.g., the fluid/solid systems, surface modes can propagate in almost all directions. With the acoustic impendence ratio approaching to one, the SAW-SAW or PSAW-PSAW gap becomes smaller. With the acoustic impendence ratio increasing to a larger value, the appearance of the SAWs becomes more difficult. For the systems with very large acoustic mismatch, only PSAW modes exist. For the systems with band gaps, the localized point-defect and the guided line-defect modes of SAWs or PSAWs can propagate.

Finally we would like to mention that the present paper still leaves some open problems; for instance, why the SAW stops at point P in Figs. 1, 6, and 8; why many scattered roots appear in Fig. 14; why the PSAW modes appear in the absolute band gaps; etc. These problems deserve extensive researches from both theoretical and experimental views.

*Corresponding author. yswang@center.njtu.edu.cn

[1] M. S. Kushwaha, P. Halevi, G. Martinez, L. Dobrzynski, and B. Djafari-Rouhani, Phys. Rev. B **49**, 2313 (1994).

[2] For an extensive list of publications on phononic crystals, refer to http://www.phys.uoa.gr/phononics

[3] M. Kafesaki and E. N. Economou, Phys. Rev. B **60**, 11993 (1999).

[4] Y. Tanaka, Y. Tomoyasu, and S. I. Tamura, Phys. Rev. B **62**, 7387 (2000).

[5] Y. Tanaka and S. I. Tamura, Phys. Rev. B **58**, 7958 (1998).

[6] Y. Tanaka and S. I. Tamura, Phys. Rev. B **60**, 13294 (1999).

[7] E. V. Tartakovskaya, Phys. Rev. B **62**, 11225 (2000).

[8] T. T. Wu, Z. G. Huang, and S. Lin, Phys. Rev. B **69**, 094301 (2004).

[9] Y. Tanaka, Y. Takafumi, and S. Tamura, Wave Motion **44**, 501 (2007).

[10] J. H. Sun and T. T. Wu, Phys. Rev. B **74**, 174305 (2006).

[11] T. T. Wu, Z. G. Huang, and S. Y. Liu, Z. Kristallogr. **220**, 841 (2005).

[12] Z. G. Huang and T.-T. Wu, Proc.-IEEE Ultrason. Symp. **1**, 77 (2005).

[13] Zi-Gui Huang and T.-T. Wu, IEEE Trans. Ultrason. Ferroelectr. Freq. Control **52**, 365 (2005).

[14] B. Manzanares-Martinez and F. Ramos-Mendieta, Phys. Rev. B **68**, 134303 (2003).

[15] M. Torres, F. R. Montero de Espinosa, D. Garcia-Pablos, and N. Garcia, Phys. Rev. Lett. **82**, 3054 (1999).

[16] A. G. Every, R. E. Vines, and J. P. Wolfe, Phys. Rev. B **60**, 11755 (1999).

[17] R. E. Vines, J. P. Wolfe, and A. V. Every, Phys. Rev. B **60**, 11871 (1999).

[18] R. E. Vines and J. P. Wolfe, Z. Kristallogr. **220**, 810 (2005).

[19] F. Meseguer, M. Holgado, D. Caballero, N. Benaches, J. Sanchez-Dehesa, C. Lopez, and J. Llinares, Phys. Rev. B **59**, 12169 (1999).

[20] V. Laude, M. Wilm, S. Benchabane, and A. Khelif, Phys. Rev. E **71**, 036607 (2005).

[21] T. T. Wu, Z. C. Hsu, and Z. G. Huang, Phys. Rev. B **71**, 064303 (2005).

[22] S. Benchabane, A. Khelif, J. Y. Rauch, L. Robert, and V. Laude, Phys. Rev. E **73**, 065601(R) (2006).

[23] Jin-Chen Hsu and T. T. Wu, IEEE Trans. Ultrason. Ferroelectr. Freq. Control **53**, 1169 (2006).

[24] Z. Z. Yan and Y. S. Wang, Phys. Rev. B **74**, 224303 (2006).